JACS
JOURNAL OF THE AMERICAN CHEMICAL SOCIETY
Article
pubs.acs.org/JACS

Titanium-Defected Undoped Anatase TiO_2 with p-Type Conductivity, Room-Temperature Ferromagnetism, and Remarkable Photocatalytic Performance

Songbo Wang,[†,‡,∥] Lun Pan,[†,‡,∥] Jia-Jia Song,[†,‡] Wenbo Mi,[§] Ji-Jun Zou,*[,†,‡] Li Wang,[†,‡] and Xiangwen Zhang[†,‡]

[†]Key Laboratory for Green Chemical Technology of the Ministry of Education, School of Chemical Engineering and Technology, Tianjin University, Tianjin 300072, China

[‡]Collaborative Innovative Center of Chemical Science and Engineering (Tianjin), Tianjin 300072, China

[§]Tianjin Key Laboratory of Low Dimensional Materials Physics and Preparation Technology, Faculty of Science, Tianjin University, Tianjin 300072, China

Supporting Information

ABSTRACT: Defects are critically important for metal oxides in chemical and physical applications. Compared with the often studied oxygen vacancies, engineering metal vacancies in n-type undoped metal oxides is still a great challenge, and the effect of metal vacancies on the physiochemical properties is seldom reported. Here, using anatase TiO_2, the most important and widely studied semiconductor, we demonstrate that metal vacancies (V_{Ti}) can be introduced in undoped oxides easily, and the presence of V_{Ti} results in many novel physiochemical properties. Anatase $Ti_{0.905}O_2$ was synthesized using solvothermal treatment of tetrabutyl titanate in an ethanol−glycerol mixture and then thermal calcination. Experimental measurements and DFT calculations on cell lattice parameters show the unstoichiometry is caused by the presence of V_{Ti} rather than oxygen interstitials. The presence of V_{Ti} changes the charge density and valence band edge of TiO_2, and an unreported strong EPR signal at $g = 1.998$ presents under room temperature. Contrary to normal n-type and nonferromagnetic TiO_2, Ti-defected TiO_2 shows inherent p-type conductivity with high charge mobility, and room-temperature ferromagnetism stronger than Co-doped TiO_2 nanocrystalline. Moreover, Ti-defected TiO_2 shows much better photocatalytic performance than normal TiO_2 in H_2 generation (4.4-fold) and organics degradation (7.0-fold for phenol), owing to the more efficient charge separation and transfer in bulk and at semiconductor/electrolyte interface. Metal-defected undoped oxides represent a unique material; this work demonstrates the possibility to fabricate such material in easy and reliable way and thus provides new opportunities for multifunctional materials in chemical and physical devices.

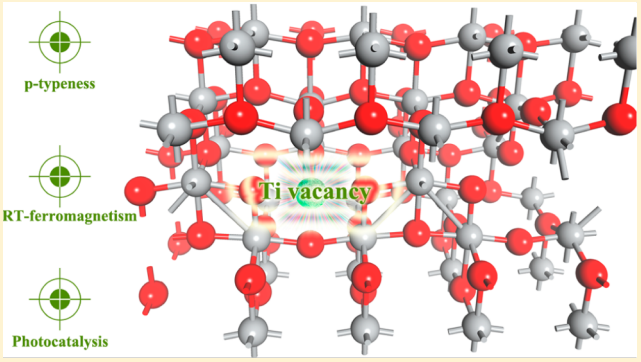

1. INTRODUCTION

The physicochemical properties of metal oxides largely depend on the concentration of intrinsic defects and extrinsic impurities, and it has been demonstrated that pure stoichiometric metal oxides are inactive in catalysis.[1−3] Defect engineering is very important to tune the functional properties of oxides, such as electronic structure, charge transport, and catalytic performance.[4,5] Specifically for semiconductors, density functional theory (DFT) calculations predict that both oxygen vacancies (V_O) and metal interstitials are shallow donors responsible for n-type conductivity, whereas metal vacancies (V_M) are shallow acceptors contributing to p-type conductivity.[6] In the past decades, V_O-related species are thought to be very important and techniques for V_O engineering have been extensively studied,[7−11] but only a few reports in the literature focus on V_M control. Although some theoretical computations have been conducted to study the role of V_M in metal oxides, experimental results are quite rare because it is quite difficult to engineer and manipulate metal defects in a stable and reliable way.[12]

Since the discovery of photoelectrochemical (PEC) water splitting in 1972,[13] anatase TiO_2 has attracted intensive attention in photocatalytic hydrogen generation, dye sensitized solar cell, pollutants removal, and CO_2 reduction.[11,14,15] Many approaches have been adopted to improve its photocatalytic performance, such as tuning oxygen defects,[16] improving the crystallinity,[17] utilizing slow photon effect,[18,19] exposing active facet,[20,21] and surface fluorination.[22,23] Actually, the photocatalytic performance of TiO_2 greatly depends on the optical and electrical properties that are mostly determined by the crystal structure and defect.[24] TiO_2 inherently exhibits n-type

Received: November 25, 2014
Published: February 6, 2015

DOI: 10.1021/ja512047k
J. Am. Chem. Soc. 2015, 137, 2975−2983

conductivity due to the existence of V_O. When the concentration of acceptor dopants increases to a suitable level,[8,25,26] the Fermi level of TiO_2 will shift toward valence band (VB) edge, and its conductivity can be altered from n- to p-type. For example, both Cr- and Fe-doped TiO_2 show p-type conductivity,[4] and Cr-doped TiO_2 photoelectrodes exhibits photocathodic current.[25] However, foreign acceptors may have a deteriorating effect on charge separation and transfer.[27,28] Titanium vacancy (V_{Ti}, Scheme 1) is acceptor type intrinsic defect, so increasing its concentration may lead to n → p transition and thus influence the mobility of charge carriers. Besides, as the only negative ionic defect in undoped TiO_2, V_{Ti} has been predicted as active site for water splitting.[7,29] However, the study on undoped anatase p-type TiO_2 is quite rare, let alone its performance in photocatalysis. Nowotny et al. reported that, annealing TiO_2 at 1323 K for 3500 h can lead to Ti-deficient oxide with p-type conductivity,[27,30] but the obtained TiO_2 is not anatase phase any more. Bhattacharyya and Basu et al. reported undoped anatase p-type TiO_2 thin films deposited on p-Si substrate, but neither checked the structure characteristic nor explained the reason for the p-type conductivity.[31−33]

Scheme 1. Representation of Different Defects in Undoped TiO_2[a]

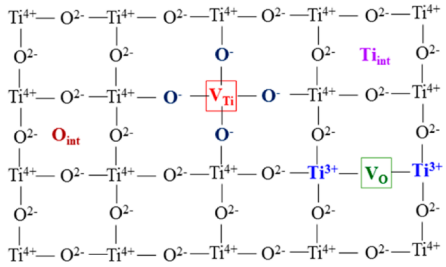

[a] V_{Ti}: Ti vacancy; V_O: oxygen vacancy; Ti_{int}: Ti interstitial; O_{int}: oxygen interstitial; Ti^{3+}: Ti^{4+} ion accepting one electron; and O^-: O^{2-} donating one electron.

Room-temperature ferromagnetic (RT-FM) oxides have attracted great interest from magnetic fluids, biomedicine, magnetic resonance imaging, catalysis, and environmental remediation.[34] The discovery of carrier mediated ferromagnetism at high temperature (~170 K) inspires numerous attempts to construct diluted magnetic semiconductors with RT-FM.[35] Koinuma et al. reported cobalt-doped anatase thin film with Curie temperature (T_C) more than 400 K.[36] But recently, debate arises on whether the ferromagnetism is really caused by the homogeneous $Ti_{1-x}Co_xO_2$ or just by the dopants themselves.[37] Meanwhile, the key of high T_C is a large density of states at the Fermi level, which is easier to achieve in p-type semiconductors.[35] Also, owing to the electronic structure changed by defects, metal-defected undoped oxides may show intrinsically high-T_C ferromagnetism.[38] Therefore, p-type metal oxide with RT-FM are potential candidates of multifunctional materials in both chemical and physical devices.

Recently, we developed a simple method to fabricate ZnO crystals abundant with Zn vacancies, and observed p-type conductivity, RT-FM, and excellent photocatalytic activity.[39] It demonstrates the possibility of reliable V_M engineering in oxides, and more importantly, suggests the resulted materials may exhibit many interesting properties that have much potential in application. This inspires us to explore the possibility of introducing V_{Ti} in TiO_2 that is the most important semiconductor oxide in both chemical and physical applications. Herein, we report the successful fabrication of undoped anatase TiO_2 abundant with V_{Ti} using simple solvothermal method, as well its structure characteristics, electrical conductivity, ferromagnetism, and photocatalytic performance, based on experiments and density functional theory simulations. The metal-defected TiO_2 represents a new kind of semiconductor and provides new opportunities for TiO_2-based materials.

2. EXPERIMENTAL SECTION

2.1. Materials. Tetrabutyl titanate [$Ti(OC_4H_9)_4$, TBT], ethanol, glycerol, methanol, $H_2PtCl_6{\cdot}6H_2O$, rhodamine B (RhB), and methyl orange (MO) were all purchased from Tianjin Guangfu Fine Chemical Research Institute, China. Phenol was obtained from J&K Chemical. Milli-Q ultra pure water with a resistivity higher than 18.2 MΩ·cm was used in all experiments. All the reagents were reagent grade and used as received.

2.2. Synthesis of Ti-Defected TiO_2. Two g TBT was added into a solution of 20 mL glycerol and 60 mL ethanol under magnetic stirring, then the solution was transferred into a 100 mL Teflon-lined autoclave and heated at 180 °C for 24 h. The obtained powders were collected, washed with absolute ethanol for several times, dried at 60 °C for 12 h, and finally calcined in air at 470 °C for 1 h with a heating rate of 5 °C/min (referred as defected TiO_2). As reference, normal TiO_2 was synthesized with the same procedure but without glycerol in the solvothermal treatment.

2.3. Structure Characterizations. XRD patterns were recorded using D/MAX-2500 X-ray diffractometer equipped with Cu Kα radiation at 40 kV and 140 mA at a scanning rate of 5°/min. TEM analysis was carried out using a Tecnai G^2 F-20 transmission electron microscope with a field-emission gun operating at 200 kV. Electron paramagnetic resonance (EPR) measurement was performed with a Bruker EMX-6/1 spectrometer at 9.424 GHz (120 K) or 9.868 GHz (298 K) using a 100 kHz field modulation and a 0.5 G standard modulation width. X-ray photoelectron spectrum (XPS) analysis was conducted with a PHI-1600 X-ray photoelectron spectroscope equipped with Al Kα radiation, and the binding energy was calibrated by the C 1s peak (284.8 eV) of contamination carbon. Ti/O ratios in bulk and on the surface were analyzed by titration method with deviation <0.5% and XPS analysis, respectively (Details are listed in the Supporting Information (SI) and Figure S1). Specific surface area (S_{BET}) was calculated based on N_2 adsorption/desorption isotherms recorded on a Micromeritics TriStar 3000 instrument at 77 K, all samples were outgassed under vacuum at 300 °C for 4 h. Steady-state photoluminescence (PL) spectra were measured by a Horiba JobinYvon Fluorolog3-21 with the excitation light at 325 nm. Positron annihilation lifetime was measured with a fast/slow coincidence ORTEC system with a time resolution of ~201 ps full width at half-maximum. A 5×10^{-5}-Bq source of ^{22}Na was sandwiched between two identical samples (10×10 mm^2, 1 mm thickness).

2.4. Measurements of Electrical and Magnetic Properties. Electrochemical properties were measured using an Autolab potentiostat/galvanostat (Model PGSTAT 302N) in a three-electrode cell with a Pt sheet as the counter electrode and an Ag/AgCl reference electrode. Na_2SO_4 (0.2 M) was used as electrolyte solution. The working electrode was prepared by dip-coating TiO_2 slurry on an F-doped tin oxide (FTO) glass electrode (1×1 cm^2) and heating it at 40 °C overnight. All investigated working electrodes were of similar thickness. Electrochemical impedance spectroscopy (EIS) measurements were carried out with a sinusoidal ac perturbation of 10 mV applied over the frequency range of $0.01-10^5$ Hz. Hall-effect measurements were carried out in the van der Pauw configuration (HL5550PC, Accent Optical Technologies Ltd., U.K.) at room temperature. The contacts were applied on the four corners of 0.5 × 0.5 cm^2 pressed pellets that were annealed at 300 °C for 1 h in air. Magnetic properties were measured using Qantum Design SQUID-

DOI: 10.1021/ja512047k
J. Am. Chem. Soc. 2015, 137, 2975−2983

VSM at a maximum field of 20 kOe in temperature range of 10−350 K.

2.5. Photocatalytic Tests. Photodegradation of organic pollutants was conducted in an opening quartz chamber (150 mL) vertically irradiated by a 300 W high-pressure xenon lamp (PLS-SXE 300UV, Beijing Trusttech. Co. Ltd.) located on the upper position. The light density was 35.2 mW/cm^2 at 365 nm, and 33.5 mW/cm^2 at 420 nm as measured with a radiometer (Photoelectric Instrument Factory, Beijin Normal University, Model UV-A). The irradiation area was ca. 20 cm^2. Reaction conditions: temperature, 25 ± 0.2 °C; C_0(RhB) = 20 μmol·L^{-1}; C_0(MO) = 120 μmol·L^{-1}; C_0(Phenol) = 400 μmol·L^{-1}; and TiO_2: 0.2 g·L^{-1}; no acid or alkaline reagents were added. For self-sensitized degradation of RhB under visible light, an UV-420 cut was equipped to eliminate UV light. Reaction was conducted by magnetic stirring under atmosphere after stirring for 20 min in darkness to achieve adsorption equilibrium. Samples were withdrawn, centrifuged, and analyzed using UV−vis spectrometer (U-3010, Hitachi Ltd.).

Photocatalytic hydrogen production was carried out in a Pyrex top-irradiation reaction vessel connected to closed glass gas system. Ten mg catalyst were dispersed in 120 mL aqueous solution containing methanol (30 vol. %). 1.0 wt. % Pt were introduced as cocatalyst by in situ photodeposition. The temperature of reaction solution was maintained at 0 °C. The resultant hydrogen was analyzed using an online gas chromatography (Bruker 450-GC, thermal conductive detector (TCD), 5 Å molecular sieve column, and N_2 as carrier gas).

2.6. Density Functional Theory Calculations. The calculations were based on density functional theory and the projector augmented wave method implemented in the Vienna Ab initio Simulation Package.[40−44] The Perdew−Burke−Ernzerhof spin-polarized generalized gradient approximation was used for the exchange-correlation potential,[43] and the plane-wave cutoff was set to 400 eV together with performing a G-centered 7 × 7 × 3 k mesh Brillouin-zone integration to obtain accurate structure for all systems. The convergence criterion for minimization of the Hellmann−Feynman force was set to less than 0.01 eV/Å.

A 2 × 2 × 1 anatase supercell was used for the calculation, with one Ti atom removed to construct Ti-defected crystal ($Ti_{15}O_{32}$, Ti/O = 0.469) and one O atom inserted in the interstitial position to construct O-interstitial crystal ($Ti_{16}O_{33}$, Ti/O = 0.485). The lattice parameters were calculated with DFT-GGA method that provides accurate lattice constants but underestimates the band gap. The GGA+U method can improve the prediction of band structure,[44] so it was applied with U = 7.2 eV for Ti atom in the static state and density of states calculation.

3. RESULTS AND DISCUSSION

3.1. Formation of Anatase TiO_2. The intermediated powders formed by solvothermal treatment of tetrabutyl titanate in glycerol-ethanol mixture show a sharp peak at 2θ = ca. 10° and several weak peaks at higher 2θ degree (SI Figure S2). Although the pattern cannot be indexed to any known structure in database, some studies refer to it as titanium glycerolate (TiGly).[45−47] The solid state CP/MAS ^{13}C NMR spectrum (SI Figure S3) shows three well resolved peaks at 73.8, 80.5, and 85.3 ppm, in accordance with the reported NMR data of TiGly.[46] From TG analysis (Figure 1a), the weight loss of the powders in the range of 200−470 °C is 52.9%, which is close to the theoretical weigh loss (52.1%) of TiGly to TiO_2.[45]

After calcination at 470 °C for 1 h, the final product (referred as defected TiO_2) can be undoubtedly identified as anatase TiO_2 (JCPDS no. 21−1272) without any other phases or impurities (Figure 1b and SI Figure S4). The sole Raman-active modes (SI Figure S5) at around 146, 399, 519, and 641 cm^{-1} confirm the formation of pure anatase phase.[48,49] TEM image (Figure 1c) shows the interplanar distances of (002) and (101) planes of anatase TiO_2,[50] which means the exposed facet is (010) facet. The fast Fourier transform pattern (inset in Figure 1d) also supports this conclusion, with the angle of 68.3° identical to the theoretical value of the angle between (101) and (001) facets.[50,51] In addition, the reference sample synthesized without glycerol (referred as normal TiO_2) is also anatase TiO_2 exposed with (101) facet, see the XRD pattern (Figure 1b) and TEM image (Figure 1d).

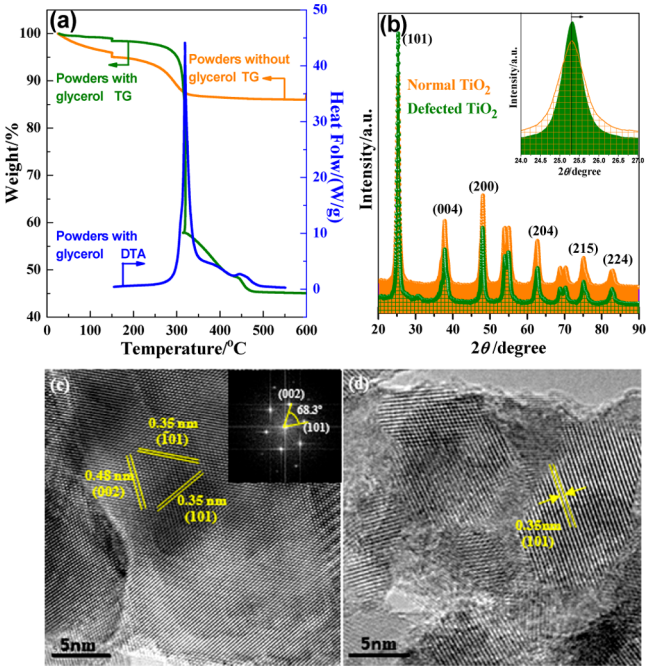

Figure 1. (a) TG and DTA profiles of intermediated powders produced by solvothermal treating TBT with and without glycerol. (b) XRD patterns of defected and normal TiO_2. Inset: Enlarged XRD patterns of peak (101). (c),(d) TEM images of defected and normal TiO_2. Inset in (c): Fast-Fourier transform pattern of defected TiO_2.

3.2. Ti Defects in TiO_2. Although the two TiO_2 samples both exhibit anatase phase, elemental analysis shows they have very different composition. As shown in Table 1, the Ti/O molar ratio in bulk determined by chemical titration is very close to the surface ratio detected by XPS, indicating that the as-prepared TiO_2 samples have homogeneous composition from the surface to inner bulk. Normal TiO_2 produced without glycerol shows nearly stoichiometric composition, but the Ti/O ratio in defected TiO_2 produced with glycerol is only 0.452, much lower than the stoichiometric ratio. Basically, there are two possibilities responsible for the unstoichiometry of defected TiO_2 (Scheme 1): Ti vacancies and/or oxygen interstitials (O_{int}).

To get more information about the defected TiO_2, EPR spectra were recorded. Under low temperature, many defect-related species and vacancies in TiO_2 can be detected. The EPR signal of Ti^{3+} defects, O_2^- and oxygen vacancies (V_O) locate at g = 1.960−1.990, 2.020, and 2.003,[10,48,52] respectively. As shown in the inset of Figure 2a, normal TiO_2 has very weak signal at g = 1.990 at 120 K, which can be assigned to the existence of trace Ti^{3+}-oxygen vacancy associates. Generally, the EPR signals of TiO_2 are visible only at sufficiently low temperature.[14,49,52,53] Surprisingly, defected TiO_2 has a remarkably strong EPR signal at g = 1.998 under both room temperature (298 K) and 120 K (Figure 2a,b). This signal cannot be indexed to any species reported in the literature, such as Ti^{3+}, O_2^-, and V_O, suggesting the formation of a new species of defects. Moreover, the Ti 2p XPS spectrum (Figure 2c) is

DOI: 10.1021/ja512047k
J. Am. Chem. Soc. 2015, 137, 2975−2983

Table 1. Lattice Constants, Molar Ratio and Electrical Properties of Normal and Defected TiO_2

samples	a (Å)	b (Å)	c (Å)	Ti/O ratio bulk	Ti/O ratio surface	resistivity $\times 10^{-4}$ (Ω cm)	mobility $\times 10^{-4}$ (cm^2/V·s)	Hall coefficient (cm^3/C)	carrier type
26−1272[a]	3.785	3.785	9.514	0.500	0.500				
normal TiO_2	3.787	3.787	9.513	0.496[c]	0.498[d]	1.497	0.223	−33.3	n
defected TiO_2	3.790	3.790	9.487	0.452[c]	0.456[d]	0.967	1.390	+134	p
$Ti_{16}O_{32}$[b]	3.804	3.804	9.481	0.500	0.500				
$Ti_{15}O_{32}$[b]	3.811	3.811	9.372	0.469	0.469				
$Ti_{16}O_{33}$[b]	3.811	3.807	9.511	0.485	0.485				

[a]Standard JCPDS card of anatase TiO_2. [b]Cluster calculated using DFT. [c]Calculated from chemical titration. [d]Calculated from XPS measurment.

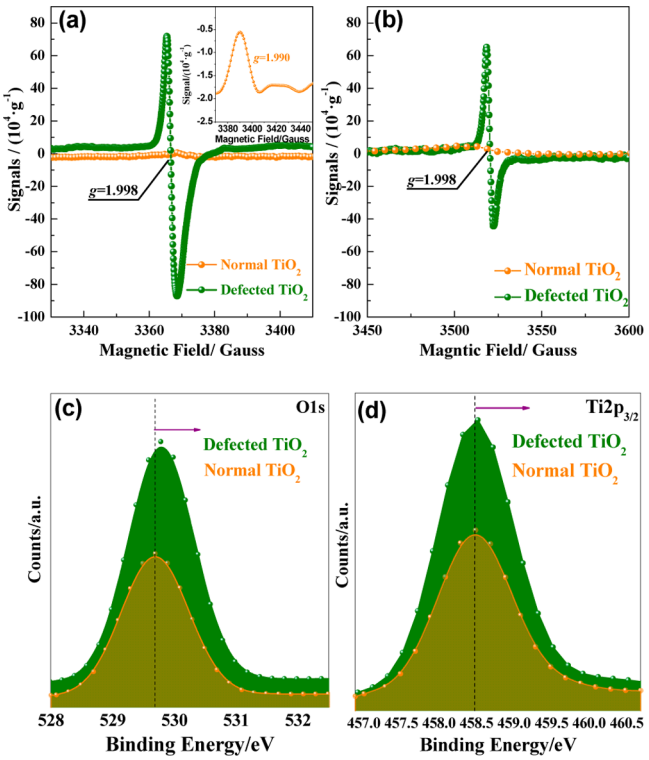

Figure 2. (a) Low temperature (120 K) and (b) room temperature (298 K) EPR spectra of defected and normal TiO_2. Inset in (a): enlarged EPR spectrum of normal TiO_2. (c) O 1s and (d) Ti $2p_{3/2}$ XPS spectra of defected and normal TiO_2.

very symmetrical, with no shoulder band appearing at 456.9 eV associated with the Ti^{3+} defect,[54] supporting that there is no Ti^{3+} and O_2^- species. In addition, the absence of peak at 457.3 eV in the Ti 2p XPS spectrum roles out the existence of Ti—H bonds,[55] and the presence of other doped impurities (mainly C atoms) is excluded by EDX and XPS analysis (SI Figure S6).

To determine the defect structure of defected TiO_2, DFT calculations on the cell structure were conducted. The optimized cell units containing V_{Ti} ($Ti_{15}O_{32}$, Ti/O = 0.469) and O_{int} ($Ti_{16}O_{33}$, Ti/O = 0.485) are shown in Figure 3, with the lattice constants summarized in Table 1. Calculation predicts that the presence of V_{Ti} makes the *c* axis to shrink heavily, whereas the *a* and *b* axes expand slightly. On the contrary, the presence of O_{int} makes the *c* axis expand. Actually, in the XRD pattern (Inset in Figure 1b), the (101) peak of defected TiO_2 is shifted toward higher angle compared with that of normal TiO_2, suggesting the lattice constants are changed. As shown in Table 1, the *c* axis of defected TiO_2 is shortened, whereas the *a* and *b* axes are elongated compared with those of normal TiO_2. This experimental result is in agreement with the computed V_{Ti} mode instead of the O_{int} mode. We further calculated the charge density of V_{Ti} mode. The neighboring O and Ti atoms of V_{Ti} get less electrons compared with those on the normal sites (Figure 3d,e), which is consistent with the increased binding energy in O 1s and Ti 2p XPS spectra of defected TiO_2 (Figure 2c,d). On the basis of the experiment and calculation, the unstoichiometry of defected TiO_2 is attributed to the presence of Ti vacancies in the lattice.

The defects in TiO_2 were further characterized by positron annihilation. As shown in SI Figure S7 and Table 2, four positron lifetime components are observed for normal and defected TiO_2. The shorter lifetime component (τ_1) is caused by the free annihilation of positrons in defect-free crystal.[56] In a disordered system, small vacancies or shallow positron traps can reduce the surrounding electron density and thus increase the lifetime of τ_1.[56−59] The τ_1 for normal and defected TiO_2 is 264 and 287 ps, respectively, longer than that of defect-free TiO_2 crystal (178 ps),[56] indicating the existence of mono-vacancies or point defects in TiO_2.[16,56−59] The very low intensity (3.0%) for normal TiO_2 corresponds to the existence of small amount of oxygen vacancies. Interestingly, the intensity of I_1 for defected TiO_2 reaches 48.5%, which indicates that the crystals have many monovacancies or point defects. Hahn et al. pointed out that metal vacancies in metal oxides exist in form of point defect.[60] In defected TiO_2, metal vacancies are the major defects. Therefore, the lifetime component of τ_1 in defected TiO_2 is attributed to Ti point vacancies. Additionally, the longer lifetime components of τ_2 and τ_3 are resulted from the positrons trapped by larger size defects, and the longest component (τ_4) is possibly due to the annihilation of orthopositronium atoms formed in the large voids present in TiO_2.[16,56]

In our recent work, Zn-defected ZnO was synthesized by calcining zinc glycerolate (ZnGly),[39] where the lamelleted structure of ZnGly plays crucial role in constructing the metal defected crystals. Actually, TiGly has parallel chains built up from edge-sharing $Ti^{4+}O_6$ octahedrals,[47,61] similar to the structure of ZnGly, so the formation mechanism of Ti vacancies should be similar to that of Zn vacancies. During calcination, interchains organic groups of TiGly is gradually removed, and the remaining Ti—O—Ti parallel lattice chains simultaneously conjunct with each other to form TiO_2 crystals. It has been reported the defects in metal oxides are sensitive to the circumstance (O- rich or metal-rich) of synthesizing process.[62−64] In particular, theoretical calculations predicted that metal vacancies can be formed easily under O-rich environment.[6,8] In the present case, the removal of interchains glycerin groups may result in O-rich environment between the

DOI: 10.1021/ja512047k
J. Am. Chem. Soc. 2015, 137, 2975−2983

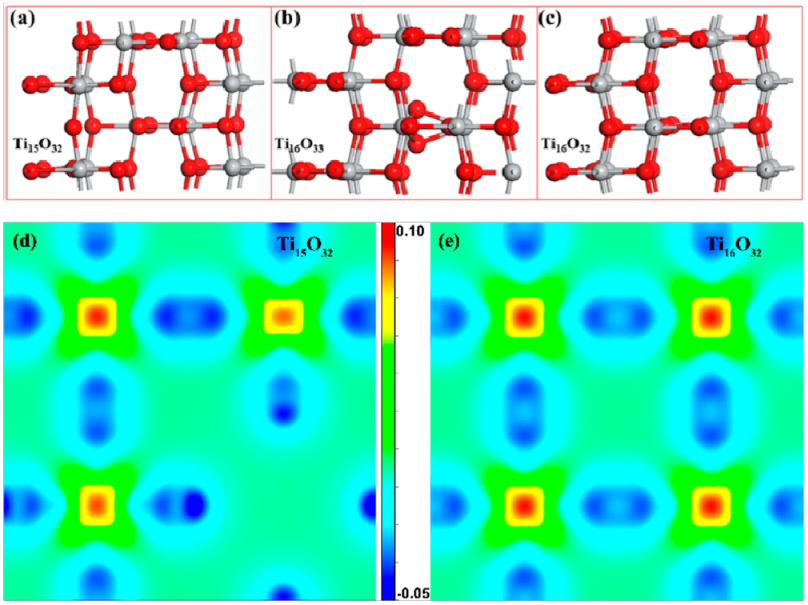

Figure 3. (a), (b), (c) Optimized cell structures of Ti-defected ($Ti_{15}O_{32}$), O-interstitial ($Ti_{16}O_{33}$), and normal anatase ($Ti_{16}O_{32}$) TiO_2, respectively. (d), (e) Charge density difference of Ti-defected ($Ti_{15}O_{32}$) and normal ($Ti_{16}O_{32}$) TiO_2, respectively.

Table 2. Positron Lifetime Parameters (Lifetime (τ), and Intensity (I)) of Normal and Defected TiO_2

samples	τ_1 (ps)	I_1 (%)	τ_2 (ps)	I_2 (%)	τ_3 (ps)	I_3 (%)	τ_4 (ns)	I_4 (%)
normal TiO_2	264	3.0	326	79.1	405	17.4	1.07	0.483
defected TiO_2	287	48.5	320	4.1	364	47.4	4.17	0.020

Ti—O—Ti parallel lattice chains, and thus metal defects are formed.

3.3. p-Type Conductivity and Room-Temperature Ferromagnetism. TiO_2 is intrinsic n-type semiconductor without any ferromagnetism. As mentioned above, V_{Ti} is acceptor-type defects, so defected TiO_2 may show p-type conductivity if the concentration of V_{Ti} is high enough. As shown in Figure 4a, the valence band of defected TiO_2 starts from 1.96 eV, which is closer to the Fermi level (0.0 eV in the valence band spectrum) compared with that of normal TiO_2 that starts from 2.12 eV, suggesting defected TiO_2 possesses p-type characteristic.[25,65]

Hall Effect measurement was conducted to get direct evidence for the type of electrical conductivity, see Table 1. The Hall coefficient is positive for defected TiO_2, which confirms this material is truly p-type and conducts via holes.[66−68] In contrast, normal TiO_2 is n-type with negative Hall coefficient. Furthermore, the presence of V_{Ti} increases the charge mobility (1.39×10^4 $cm^2/V{\cdot}s$ for defected TiO_2 vs 2.23×10^3 $cm^2/V{\cdot}s$ for normal TiO_2). It was reported that the mobility of Mn-doped p-TiO_2 is lower than that of pure TiO_2.[28] Unlike foreign p-type dopants, V_{Ti} has no deteriorating effect on the charge transfer.

The electrochemical impedance measurements and photoelectrochemical characterizations were also performed to determine the conductivity of defected TiO_2. The evidence for p-type conductivity comes from the negative slope of linear part of Mott−Schottky plots (Figure 4b).[69] Correspondingly, defected TiO_2 photocathode shows obvious cathodic current under illumination (Figure 4c) with the photocurrent increasing progressively with the increase of negative potential applied (due to increased band bending), also see the transient current (I−t) curves (Inset in Figure 4c) with a sharp cathodic current peak appears upon the turn-on of light. On the contrary, normal TiO_2 exhibits positive slope in the Mott−Schottky plots (SI Figure S8) and do not show any cathodic current under similar measurement conditions (Figure 4c). Besides, the photocurrent onset potential (−0.40 V vs Ag/AgCl) of defected TiO_2 is more negative than the V_{FB}, which is also consistent with the feature of p-type photoelectrode.[70]

DFT calculations indicate that the presence of V_{Ti} in TiO_2 causes ferromagnetism (SI Table S1). The magnetic response was measured as a function of magnetic field strength (M−H) at 300 K (Figure 5a). A well-defined hysteresis loop is observed, indicating that the defected TiO_2 crystal is ferromagnetic at room temperature. From the M−T curve in a field of 4000 Oe (Figure 5b), the Curie temperature is higher than 300 K. The spontaneous magnetic moment deduced from the saturated magnetization value is 0.025 $emu{\cdot}g^{-1}$, and the coercivity is about 18 Oe, which is significantly higher than the reported magnetization of Co-doped TiO_2 nanocrystalline ($Ti_{0.985}Co_{0.15}O_2$, 1.57×10^{-3} $emu{\cdot}g^{-1}$).[71] In addition, according to DFT calculation (SI Table S1,), the O_{int} mode does not have any ferromagnetism.

3.4. Photocatalytic Performance. TiO_2 is the most widely studied photocatalyst in energy and environment fields. Here we tested the photocatalytic activity of defected TiO_2 in three types of reactions: H_2 generation under UV light, organic pollutant (RhB, MO, and phenol) degradation under UV light, and self-sensitized RhB degradation under visible light. The photoreaction under UV light involves the formation, separation, and transfer of electron−hole pairs, surface reaction, with charge recombination as the major side process,[24] The sensitized reaction under visible light involves the excitation of dye, injection of electron from dye to TiO_2, and then surface reaction, with the electron back-injection as the side process.[15]

DOI: 10.1021/ja512047k
J. Am. Chem. Soc. 2015, 137, 2975−2983

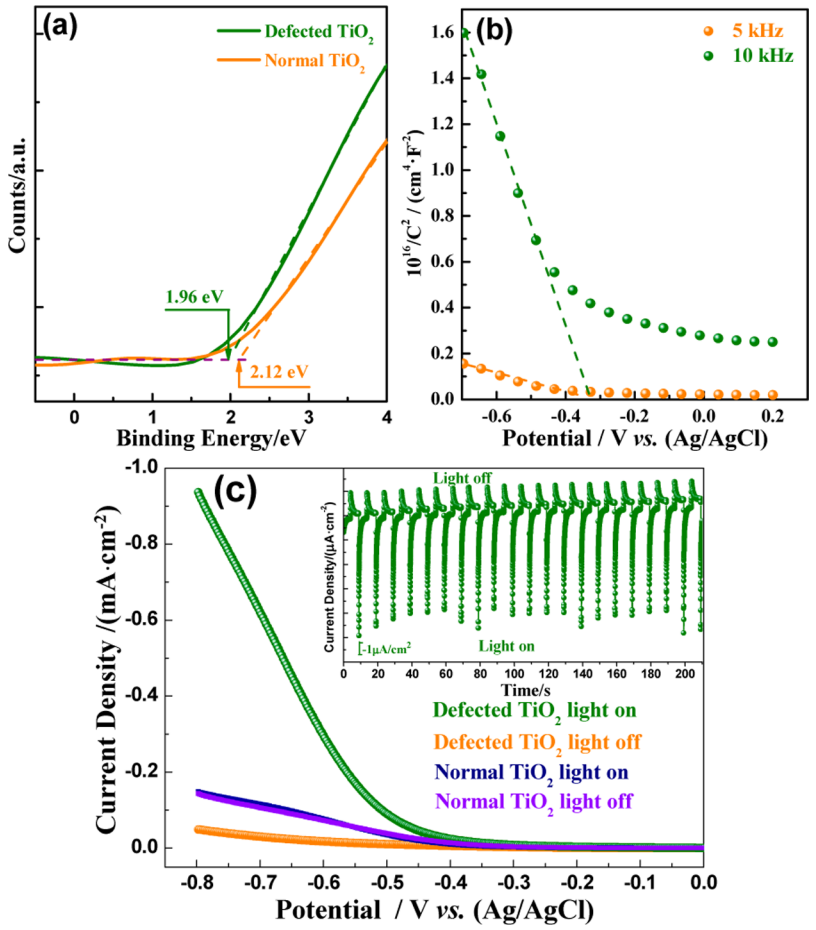

Figure 4. (a) XPS valence band spectra of defected and normal TiO_2. (b) Mott−Schottky plots measured in a standard three-electrode setup using defected TiO_2 electrode as working electrode. (c) Current−voltage (I−V) curve of defected and normal TiO_2, inset in (c): transient photocurrent (chronoamperometric) curve of defected TiO_2 at −0.45 V vs Ag/AgCl.

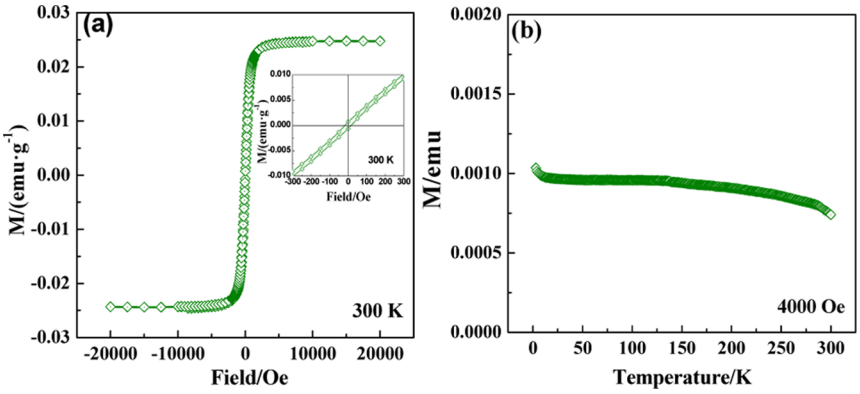

Figure 5. (a) Magnetization (M−H) curves of defected TiO_2 measured at 300 K. (b) M−T curve of defected TiO_2 in the field of 4000 Oe.

No matter what type the photocatalysis is, the charge transfer in TiO_2 crystal is one key factor determining the efficiency.

The reaction rate shown in Figure 6a derived from pseudo-first-order fitting of data in SI Figure S9 is used to evaluate the degradation photoactivity. Obviously, defected TiO_2 is much more active than normal TiO_2 under both UV and visible illumination. The phenol degradation rate of defected TiO_2 is 7.0-fold of normal TiO_2. Figure 6b shows the time course of H_2 evolution, defected TiO_2 exhibits stable H_2 release rate of 29.8 mmol·g^{-1}·h^{-1}, whereas normal TiO_2 produces only 6.8 mmol·g^{-1}·h^{-1} under the same conditions.

Defected and normal TiO_2 are both pure anatase phase, and have similar morphology (SI Figure S10), comparable BET surface area (59 m^2·g^{-1} and 72 m^2·g^{-1} for normal and defected TiO_2, respectively) and identical optical absorption (SI Figure S11), so the influences of morphology, surface area, and optical property on the photoactivity are excluded. The only difference is the presence of metal defects in defected TiO_2. Actually, it has been reported that increasing the concentration of Ti vacancies can increase the electrical conductivity and the mobility of electronic charge carriers.[29] More specifically, as shown in Figure 7a, the calculated density of states (DOS) of

DOI: 10.1021/ja512047k
J. Am. Chem. Soc. 2015, 137, 2975−2983

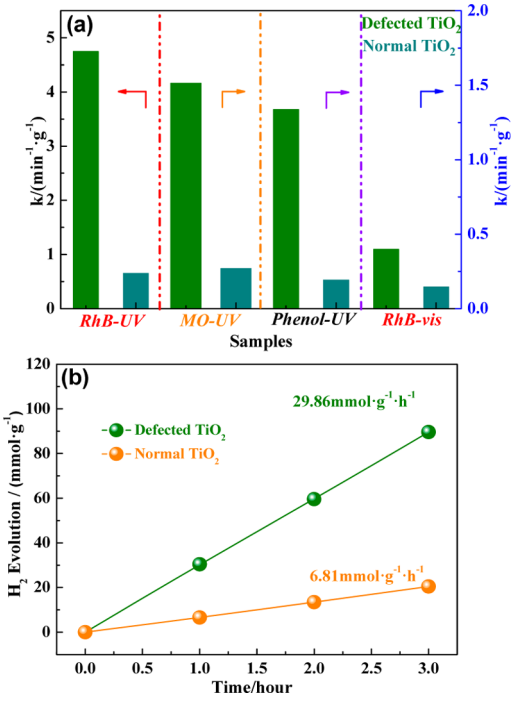

Figure 6. (a) Reaction rate of photodegradation of organic pollutants. (b) Time course of hydrogen generation.

defected TiO_2 has a new band transition above the top of original VB, which means the VB width is raised. The VB width intrinsically controls the mobility of holes, and wider VB results in higher mobility of holes generated.[72,73] Therefore, the charge transfer and separation in defected TiO_2 is improved.

The more efficient charge transfer and separation of defected TiO_2 is confirmed by experiments. The photoluminescence (PL) emission signal caused by charge recombination can reflect the charge separation in bulk. As shown in Figure 7b, defected TiO_2 has smaller PL intensity than normal TiO_2, which indicates a more efficient transfer and separation of photoinduced charge pairs. In electrochemical impedance spectroscopy, the radius of arc of Nyquist plots can be used to evaluate the charge transfer resistance at the semiconductor/electrolyte interface, and smaller arc radius implies smaller charge transfer resistance.[74] Figure 7c shows that defected TiO_2 exhibits smaller radius, so the charge in defected TiO_2 can be quickly transferred to reactant through the solid/liquid interface and consumed by chemical reaction. The quick consumption of surface charges in turn retards the charge recombination or back charge transfer side processes.

The stability of surface defects is important because photocatalysis is very sensitive to them. XPS analysis reveals the surface Ti/O ratio, binding energies of Ti, and lattice O of defected TiO_2 do not change after 4 months storage under atmosphere (SI Figure S12). Moreover, defected TiO_2 shows stable activity in 5 recycles of photocatalytic reactions (SI

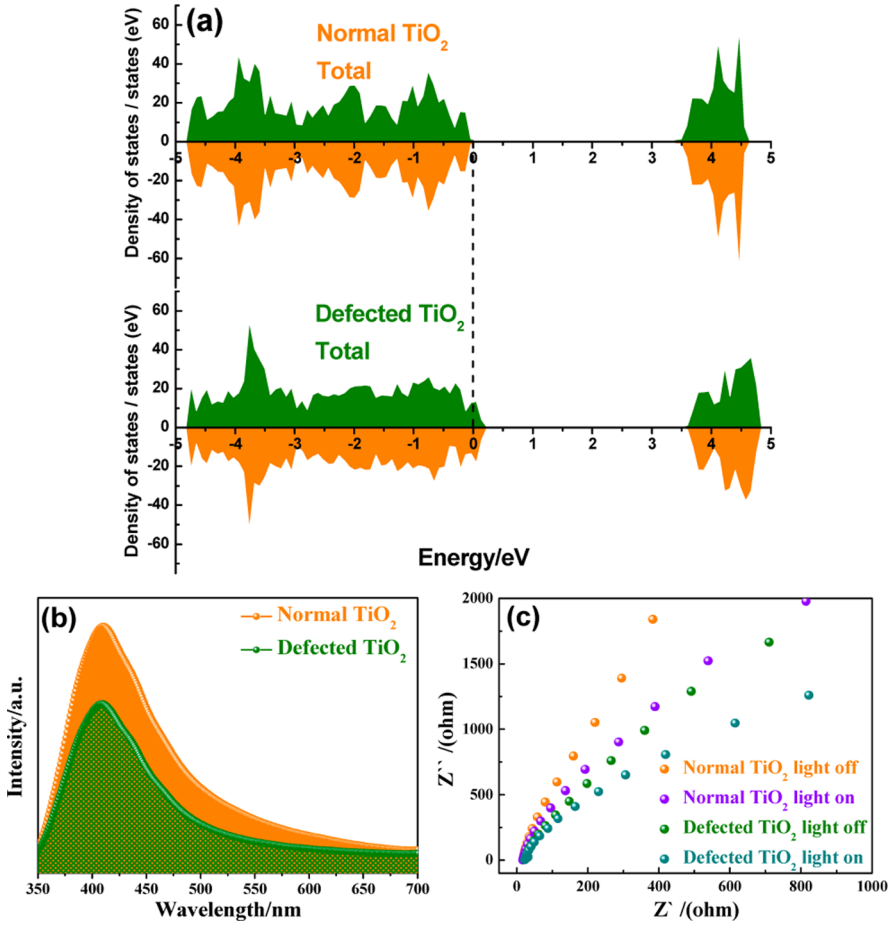

Figure 7. (a) Calculated total density of states of normal TiO_2 ($Ti_{16}O_{32}$) and defected TiO_2 ($Ti_{15}O_{32}$), (b) steady state PL spectra of defected and normal TiO_2, and (c) EIS Nyquist plot of defected and normal TiO_2.

DOI: 10.1021/ja512047k
J. Am. Chem. Soc. 2015, 137, 2975−2983

Figure S13), and the surface defects are well retained after the recycling, as evidenced by XPS analysis (SI Figure S12). These results indicate that the surface defects are stable under the reaction conditions and long-term storage.

4. CONCLUSIONS

We successfully synthesized undoped anatase TiO_2 with large amount of (9.5 mol %) Ti vacancies using a solvothermal treatment method. The presence of abundant V_{Ti} makes the *c* axis of anatase shrink heavily, whereas the *a* and *b* axes elongated slightly, generates a strong EPR signal at $g = 1.998$ even under room temperature, and widens the valence band top edge. V_{Ti} switches TiO_2 conductivity from n-type to p-type with higher charge mobility, and endows room temperature ferromagnetism stronger than Co-doped TiO_2 nanocrystalline. Moreover, defected TiO_2 exhibits remarkably higher photocatalytic activity compared with normal TiO_2 because of the more efficient charge transfer in bulk and at semiconductor/electrolyte interface. It indicates that the metal vacancies can change the structure characteristics and physiochemical properties of undoped semiconductor and thus produce a new kind of functional materials for chemical and physical devices.

■ ASSOCIATED CONTENT

Supporting Information

Details of composition analysis, XRD pattern of intermediated powders, NMR spectra of TiGly, XPS spectrum, positron annihilation spectra, EDS spectra, Raman spectra, computed ferromagnetism of defected TiO_2, UV−vis DRS spectra, photodegradation data, stability test, and SEM images. This material is available free of charge via the Internet at http://pubs.acs.org.

■ AUTHOR INFORMATION

Corresponding Author

jj_zou@tju.edu.cn

Author Contributions

‖These authors contributed equally.

Notes

The authors declare no competing financial interest.

■ ACKNOWLEDGMENTS

The authors appreciate the supports from the National Natural Science Foundation of China (21222607, U1463205), the Tianjin Municipal Natural Science Foundation, and the Program for New Century Excellent Talents in Universities (NCET-09-0594).

■ REFERENCES

(1) Gray, T. J.; McCain, C. C.; Masse, N. G. *J. Phys. Chem.* **1959**, *63*, 472−475.
(2) Henrich, V. E.; Dresselhaus, G.; Zeiger, H. J. *Phys. Rev. Lett.* **1976**, *36*, 1335−1339.
(3) Brown, G. E. Jr; Henrich, V. E.; Casey, W. H.; Clark, D. L.; Eggleston, C.; Felmy, A.; Goodman, D. W.; Grätzel, M.; Maciel, G.; McCarthy, M. I.; Nealson, K. H.; Sverjensky, D. A.; Toney, M. F.; Zachara, J. M. *Chem. Rev.* **1999**, *99*, 77−174.
(4) Bally, A. R.; Korobeinikova, E. N.; Schmid, P. E.; Levy, F.; Bussy, F. *J. Phys. D: Appl. Phys.* **1998**, *31*, 1149−1154.
(5) Nowotny, M. K.; Sheppard, L. R.; Bak, T.; Nowotny, J. *J. Phys. Chem. C* **2008**, *112*, 5275−5300.
(6) Morgan, B. J.; Watson, G. W. *Phys. Rev. B* **2009**, *80*, 233102.
(7) Nowotny, J.; Bak, T.; Nowotny, M. K.; Sheppard, L. R. *J. Phys. Chem. B* **2006**, *110*, 18492−18495.
(8) Na-Phattalung, S.; Smith, M. F.; Kim, K.; Du, M.-H.; Wei, S.-H.; Zhang, S. B.; Limpijumnong, S. *Phys. Rev. B* **2006**, *73*, 125205.
(9) Hong, N. H.; Sakai, J.; Poirot, N.; Brize, V. *Phys. Rev. B* **2006**, *73*, 132404.
(10) Wang, W.; Ni, Y.; Lu, C.; Xu, Z. *RSC Adv.* **2012**, *2*, 8286−8288.
(11) Lira, E.; Wendt, S.; Huo, P.; Hansen, J. O.; Streber, R.; Porsgaard, S.; Wei, Y.; Bechstein, R.; Laegsgaard, E.; Besenbacher, F. *J. Am. Chem. Soc.* **2011**, *133*, 6529−6532.
(12) Coey, J. M. D.; Venkatesan, M.; Fitzgerald, C. B. *Nat. Mater.* **2005**, *4*, 173−179.
(13) Fujishima, A.; Honda, K. *Nature* **1972**, *238*, 37−38.
(14) Zuo, F.; Bozhilov, K.; Dillon, R. J.; Wang, L.; Smith, P.; Zhao, X.; Bardeen, C.; Feng, P. *Angew. Chem., Int. Ed.* **2012**, *51*, 6223−6226.
(15) Pan, L.; Zou, J.-J.; Zhang, X.; Wang, L. *J. Am. Chem. Soc.* **2011**, *133*, 10000−10002.
(16) Kong, M.; Li, Y.; Chen, X.; Tian, T.; Fang, P.; Zheng, F.; Zhao, X. *J. Am. Chem. Soc.* **2011**, *133*, 16414−16417.
(17) Zhou, W.; Sun, F.; Pan, K.; Tian, G.; Jiang, B.; Ren, Z.; Tian, C.; Fu, H. *Adv. Funct. Mater.* **2011**, *21*, 1922−1930.
(18) Li, Y.; Kunitake, T.; Fujikawa, S. *J. Phys. Chem. B* **2006**, *110*, 13000−13004.
(19) Wu, M.; Jin, J.; Liu, J.; Deng, Z.; Li, Y.; Depairs, O.; Su, B.-L. *J. Mater. Chem. A* **2013**, *1*, 15491−15500.
(20) Yang, H. G.; Sun, C. H.; Qiao, S. Z.; Zou, J.; Liu, G.; Smith, S. C.; Cheng, H. M.; Lu, G. Q. *Nature* **2008**, *453*, 638−641.
(21) Liu, S.; Yu, J.; Jaroniec, M. *J. Am. Chem. Soc.* **2010**, *132*, 11914−11916.
(22) Ren, L.; Li, Y.; Hou, J.; Zhao, X.; Pan, C. *ACS Appl. Mater. Interfaces* **2014**, *6*, 1608−1615.
(23) Xiang, Q.; Lv, K.; Yu, J. *Appl. Catal., B* **2010**, *96*, 557−564.
(24) Liu, G.; Yang, H. G.; Pan, J.; Yang, Y. Q.; Lu, G. Q.; Cheng, H.-M. *Chem. Rev.* **2014**, *114*, 9559−9612.
(25) Cao, J.; Zhang, Y.; Liu, L.; Ye, J. *Chem. Commun.* **2013**, *49*, 3440−3442.
(26) Ruiz, A.; Cornet, A.; Sakai, G.; Shimanoe, K.; Morante, J. R.; Yamazoe, N. *Chem. Lett.* **2002**, *31*, 892−893.
(27) Nowotny, M. K.; Bak, T.; Nowotny, J.; Sorrell, C. C. *Phys. Stat. Solidi B* **2005**, *242*, R88−R90.
(28) Li, X.; Wu, S.; Hu, P.; Xing, X.; Liu, Y.; Yu, Y.; Yang, M.; Lu, J.; Li, S.; Liu, W. *J. Appl. Phys.* **2009**, *106*, 043913.
(29) Bak, T.; Nowotny, M. K.; Sheppard, L. R.; Nowotny, J. *J. Phys. Chem. C* **2008**, *112*, 13248−13257.
(30) Nowotny, M. K.; Bogdanoff, P.; Dittrich, T.; Fiechter, S.; Fujishima, A.; Tributsch, H. *Mater. Lett.* **2010**, *64*, 928−930.
(31) Bhowmik, B.; Dutta, K.; Hazra, A.; Bhattacharyya, P. *Solid-State Electron.* **2014**, *99*, 84−92.
(32) Hazra, A.; Das, S.; Kanungo, J.; Sarkar, C. K.; Basu, S. *Sens. Actuators, B* **2013**, *183*, 87−95.
(33) Hazra, A.; Das, S.; Kanungo, J.; Bontempi, E.; Sarkar, C. K.; Bhattacharyya, P.; Basu, S. *J. Mater. Sci.: Mater. Electron.* **2013**, *24*, 1658−1663.
(34) Lu, A.-H.; Salabas, E. L.; Schüth, F. *Angew. Chem., Int. Ed.* **2007**, *46*, 1222−1244.
(35) Chambers, S. A. *Surf. Sci. Rep.* **2006**, *61*, 345−381.
(36) Matsumoto, Y.; Murakami, M.; Shono, T.; Hasegawa, T.; Fukumura, T.; Kawasaki, M.; Ahmet, P.; Chikyow, T.; Koshihara, S.; Koinuma, H. *Science* **2001**, *291*, 854−856.
(37) Sharma, P.; Gupta, A.; Rao, K. V.; Owens, F. J.; Sharma, R.; Ahuja, R.; Guillen, J. M. O.; Johansson, B.; Gehring, G. A. *Nat. Mater.* **2003**, *2*, 673−677.
(38) Janotti, A.; Van de Walle, C. G. *Phys. Rev. B* **2007**, *76*, 165202.
(39) Pan, L.; Wang, S.; Mi, W.; Song, J.; Zou, J.-J.; Wang, L.; Zhang, X. *Nano Energy* **2014**, *9*, 71−79.
(40) Kohn, W.; Sham, L. J. *Phys. Rev.* **1965**, *140*, A1133−A1138.
(41) Blöchl, P. E. *Phys. Rev. B* **1994**, *50*, 17953−17979.
(42) Kresse, G.; Furthmüller, J. *Phys. Rev. B* **1996**, *54*, 11169−11186.

DOI: 10.1021/ja512047k
J. Am. Chem. Soc. 2015, 137, 2975−2983

(43) Perdew, J. P.; Burke, K.; Ernzerhof, M. *Phys. Rev. Lett.* **1996**, *77*, 3865−3868.
(44) Dudarev, S. L.; Botton, G. A.; Savrasov, S. Y.; Humphreys, C. J.; Sutton, A. P. *Phys. Rev. B* **1998**, *57*, 1505−1509.
(45) Zakharova, G. S.; Andreikov, E. I.; Osipova, V. A.; Yatluk, Y. G.; Puzyrev, I. S. *Inorg. Mater.* **2013**, *49*, 1127−1132.
(46) Chen, Y.; Tian, G.; Ren, Z.; Tian, C.; Pan, K.; Zhou, W.; Fu, H. *Eur. J. Inorg. Chem.* **2011**, *2011*, 754−760.
(47) Zhao, J.; Liu, Y.; Fan, M.; Yuan, L.; Zou, X. *Inorg. Chem. Front.* **2015**, DOI: 10.1039/C4QI00191E.
(48) Yu, X.; Kim, B.; Kim, Y. K. *ACS Catal.* **2013**, *3*, 2479−2486.
(49) Pan, L.; Zou, J.-J.; Wang, S.; Huang, Z.-F.; Yu, A.; Wang, L.; Zhang, X. *Chem. Commun.* **2013**, *49*, 6593−6595.
(50) Zhao, J.; Zou, X. X.; Su, J.; Wang, P. P.; Zhou, L. J.; Li, G. D. *Dalton Trans.* **2013**, *42*, 4365−4368.
(51) Pan, L.; Zou, J.-J.; Wang, S.; Liu, X.-Y.; Zhang, X.; Wang, L. *ACS Appl. Mater. Interfaces* **2012**, *4*, 1650−1655.
(52) Liu, H.; Ma, H. T.; Li, X. Z.; Li, W. Z.; Wu, M.; Bao, X. H. *Chemosphere* **2003**, *50*, 39−46.
(53) Naldoni, A.; Allieta, M.; Santangelo, S.; Marelli, M.; Fabbri, F.; Cappelli, S.; Bianchi, C. L.; Psaro, R.; Dal Santo, V. *J. Am. Chem. Soc.* **2012**, *134*, 7600−7603.
(54) Wang, R.; Sakai, N.; Fujishima, A.; Watanabe, T.; Hashimoto, K. *J. Phys. Chem. B* **1999**, *103*, 2188−2194.
(55) Zheng, Z.; Huang, B.; Lu, J.; Wang, Z.; Qin, X.; Zhang, X.; Dai, Y.; Whangbo, M.-H. *Chem. Commun.* **2012**, *48*, 5733−5735.
(56) Murakami, H.; Onizuka, N.; Sasaki, J.; Thonghai, N. *J. Mater. Sci.* **1998**, *33*, 5811−5814.
(57) Yan, J.; Wu, G.; Guan, N.; Li, L.; Li, Z.; Cao, X. *Phys. Chem. Chem. Phys.* **2013**, *15*, 10978−10988.
(58) Jiang, X.; Zhang, Y.; Jiang, J.; Rong, Y.; Wang, Y.; Wu, Y.; Pan, C. *J. Phys. Chem. C* **2012**, *116*, 22619−22624.
(59) Zheng, F.; Liu, Y.; Liu, Z.; Dai, Y. Q.; Fang, P. F.; Wang, S. J. *J. Cryst. Growth* **2012**, *353*, 55−58.
(60) Hahn, B. P.; Long, J. W.; Rolison, D. R. *Acc. Chem. Res.* **2013**, *46*, 1181−1191.
(61) Wang, D.; Yu, R.; Kumada, N.; Kinomura, N. *Chem. Mater.* **1999**, *11*, 2008−2012.
(62) Zhang, S.; Ogale, S. B.; Yu, W.; Gao, X.; Liu, T.; Ghosh, S.; Das, G. P.; Wee, A. T. S.; Greene, R. L.; Venkatesan, T. *Adv. Mater.* **2009**, *21*, 2282−2287.
(63) Wang, X. F.; Xu, J. B.; Zhang, B.; Yu, H. G.; Wang, J.; Zhang, X.; Yu, J. G.; Li, Q. *Adv. Mater.* **2006**, *18*, 2476−2480.
(64) Xiang, B.; Wang, P.; Zhang, X.; Dayeh, S. A.; Aplin, D. P. R.; Soci, C.; Yu, D.; Wang, D. *Nano Lett.* **2007**, *7*, 323−328.
(65) Li, X.; Guo, Z.; He, T. *Phys. Chem. Chem. Phys.* **2013**, *15*, 20037−20045.
(66) Kawazoe, H.; Yasukawa, M.; Hyodo, H.; Kurita, M.; Yanagi, H.; Hosono, H. *Nature* **1997**, *389*, 939−942.
(67) Look, D. C.; Reynolds, D. C.; Litton, C. W.; Jones, R. L.; Eason, D. B.; Cantwell, G. *Appl. Phys. Lett.* **2002**, *81*, 1830−1832.
(68) Bian, J. M.; Li, X. M.; Gao, X. D.; Yu, W. D.; Chen, L. D. *Appl. Phys. Lett.* **2004**, *84*, 541−543.
(69) Lin, Y.; Xu, Y.; Mayer, M. T.; Simpson, Z. I.; McMahon, G.; Zhou, S.; Wang, D. *J. Am. Chem. Soc.* **2012**, *134*, 5508−5511.
(70) Scragg, J. J.; Dale, P. J.; Peter, L. M.; Zoppi, G.; Forbes, I. *Phys. Stat. Solidi B* **2008**, *245*, 1772−1778.
(71) Bryan, J. D.; Heald, S. M.; Chambers, S. A.; Gamelin, D. R. *J. Am. Chem. Soc.* **2004**, *126*, 11640−11647.
(72) Liu, G.; Niu, P.; Sun, C.; Smith, S. C.; Chen, Z.; Lu, G. Q.; Cheng, H.-M. *J. Am. Chem. Soc.* **2010**, *132*, 11642−11648.
(73) Guan, M.; Xiao, C.; Zhang, J.; Fan, S.; An, R.; Cheng, Q.; Xie, J.; Zhou, M.; Ye, B.; Xie, Y. *J. Am. Chem. Soc.* **2013**, *135*, 10411−10417.
(74) Huang, Z.-F.; Song, J.; Pan, L.; Jia, X.; Li, Z.; Zou, J.-J.; Zhang, X.; Wang, L. *Nanoscale* **2014**, *6*, 8865−8872.

DOI: 10.1021/ja512047k
J. Am. Chem. Soc. 2015, 137, 2975−2983